nature astronomy

LETTERS

https://doi.org/10.1038/s41550-019-1007-5

The violent collisional history of aqueously evolved (2) Pallas

Michaël Marsset[1,2]*, Miroslav Brož[3], Pierre Vernazza[4], Alexis Drouard[4], Julie Castillo-Rogez[5], Josef Hanuš[3], Matti Viikinkoski[6], Nicolas Rambaux[7], Benoît Carry[8], Laurent Jorda[4], Pavel Ševeček[3], Mirel Birlan[7,9], Franck Marchis[10], Edyta Podlewska-Gaca[11,12], Erik Asphaug[13], Przemyslaw Bartczak[11], Jérôme Berthier[7], Fabrice Cipriani[14], François Colas[7], Grzegorz Dudziński[11], Christophe Dumas[15], Josef Ďurech[3], Marin Ferrais[4,16], Romain Fétick[4], Thierry Fusco[4,17], Emmanuel Jehin[16], Mikko Kaasalainen[6], Agnieszka Kryszczynska[11], Philippe Lamy[4], Hervé Le Coroller[4], Anna Marciniak[11], Tadeusz Michalowski[11], Patrick Michel[8], Derek C. Richardson[18], Toni Santana-Ros[19,20], Paolo Tanga[8], Frédéric Vachier[7], Arthur Vigan[4], Olivier Witasse[14] and Bin Yang[21]

Asteroid (2) Pallas is the largest main-belt object not yet visited by a spacecraft, making its surface geology largely unknown and limiting our understanding of its origin and collisional evolution. Previous ground-based observational campaigns returned different estimates of its bulk density that are inconsistent with one another, one measurement[1] being compatible within error bars with the icy Ceres ($2.16 \pm 0.01\,\mathrm{g\,cm^{-3}}$)[2] and the other[3] compatible within error bars with the rocky Vesta ($3.46 \pm 0.03\,\mathrm{g\,cm^{-3}}$)[4]. Here we report high-angular-resolution observations of Pallas performed with the extreme adaptive optics-fed SPHERE imager[5] on the Very Large Telescope. Pallas records a violent collisional history, with numerous craters larger than 30 km in diameter populating its surface and two large impact basins that could be related to a family-forming impact. Monte Carlo simulations of the collisional evolution of the main belt correlate this cratering record to the high average impact velocity of ~11.5 km s^{-1} on Pallas—compared with an average of ~5.8 km s^{-1} for the asteroid belt—induced by Pallas's high orbital inclination ($i = 34.8°$) and orbital eccentricity ($e = 0.23$). Compositionally, Pallas's derived bulk density of $2.89 \pm 0.08\,\mathrm{g\,cm^{-3}}$ (1σ uncertainty) is fully compatible with a CM chondrite-like body, as suggested by its spectral reflectance in the 3 µm wavelength region[6]. A bright spot observed on its surface may indicate an enrichment in salts during an early phase of aqueous alteration, compatible with Pallas's relatively high albedo of 12–17% (refs. [7,8]), although alternative origins are conceivable.

We used the sharp angular resolution (~20 mas at 600 nm) of the Spectro-Polarimetric High-contrast Exoplanet REsearch (SPHERE)/ Zurich IMaging POLarimeter (ZIMPOL) camera on the Very Large Telescope (VLT)[5,9] to characterize Pallas's bulk shape and surface properties with unprecedented detail and, in turn, to bring new constraints on its origin and evolution. In total, 11 series of images were acquired during two apparitions as part of an European Southern Observatory (ESO) large programme[10]. These images provide a full surface coverage, resolving ~120 to 130 pixels along Pallas's longest axis. The optimal angular resolution of each image was restored with Mistral[11,12], a myopic deconvolution algorithm optimized for images of objects with sharp boundaries, using a parametric point spread function[13].

The deconvolved images unveil a strong surface topographic relief suggestive of a violent collisional history (Fig. 1). Numerous large (~30–120-km-sized) impact features, including several craters with central peaks (Supplementary Fig. 1), are ubiquitous on Pallas, forming a surface reminiscent of a 'golf ball'. A total of 36 craters larger than 30 km in diameter (D_c) identified on the images (Figs. 2 and 3 and Supplementary Table 1) implies an observed average number density of $N\,(D_c \geq 40\,\mathrm{km}) = (4.8 \pm 0.7) \times 10^{-5}\,\mathrm{km^{-2}}$. The region with most favourable illumination in our observations (Fig. 3) is more than three times more cratered than this average, with $N\,(D_c \geq 40\,\mathrm{km}) = (1.6 \pm 0.2) \times 10^{-4}\,\mathrm{km^{-2}}$, which seems comparable to the most heavily cratered geological units on Ceres[14] and Vesta[15] (Methods). The similar maximum crater densities on Ceres, Pallas and Vesta could indicate some degree of saturation in this diameter range. It should be noted, however, that observed $D_c \geq 40$ km craters are relatively depleted on Ceres and Vesta, and the reported crater density values in this size range are often extrapolated from the observed number of smaller ($D_c \geq 1$ km) craters by use of a model

---

[1]Department of Earth, Atmospheric and Planetary Sciences, MIT, Cambridge, MA, USA. [2]Astrophysics Research Centre, Queen's University Belfast, Belfast, UK. [3]Institute of Astronomy, Charles University, Prague, Czech Republic. [4]Aix Marseille Univ, CNRS, CNES, Laboratoire d'Astrophysique de Marseille, Marseille, France. [5]Jet Propulsion Laboratory, California Institute of Technology, Pasadena, CA, USA. [6]Mathematics and Statistics, Tampere University, Tampere, Finland. [7]IMCCE, Observatoire de Paris, Paris, France. [8]Université Côte d'Azur, Observatoire de la Côte d'Azur, CNRS, Laboratoire Lagrange, Nice, France. [9]Astronomical Institute of the Romanian Academy, Bucharest, Romania. [10]SETI Institute, Carl Sagan Center, Mountain View, CA, USA. [11]Astronomical Observatory Institute, Faculty of Physics, Adam Mickiewicz University, Poznań, Poland. [12]Institute of Physics, University of Szczecin, Szczecin, Poland. [13]School of Earth and Space Exploration, Arizona State University, Tempe, AZ, USA. [14]European Space Agency, ESTEC – Scientific Support Office, Noordwijk, The Netherlands. [15]TMT Observatory, Pasadena, CA, USA. [16]Space Sciences, Technologies and Astrophysics Research Institute, Université de Liège, Liège, Belgium. [17]ONERA, The French Aerospace Lab, Châtillon, France. [18]Department of Astronomy, University of Maryland, College Park, MD, USA. [19]Departamento de Física, Ingeniería de Sistemas y Teoría de la Señal, Universidad de Alicante, Alicante, Spain. [20]Institut de Ciències del Cosmos, Universitat de Barcelona (IEEC-UB), Barcelona, Spain. [21]European Southern Observatory (ESO), Santiago, Chile. *e-mail: mmarsset@mit.edu

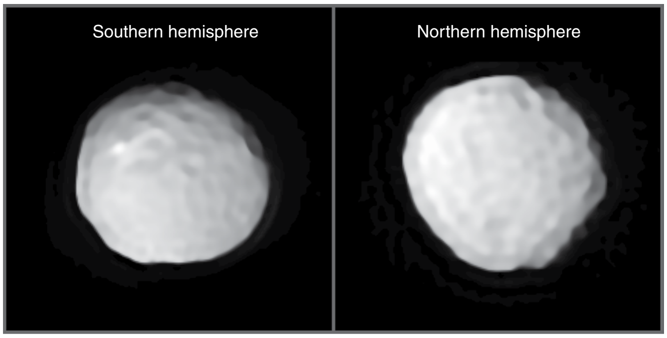

Fig. 1 | The two hemispheres of (2) Pallas as seen by VLT/SPHERE. Images taken on 28 October 2017 UT (southern hemisphere) and 15 March 2019 UT (northern hemisphere). Numerous large craters are visible on both hemispheres, and a bright spot reminiscent of salt deposits on Ceres is found on the southern one.

production function[16]. In the case of Pallas, large craters are directly detected and cover a notable fraction (at least 9%) of the total surface.

To understand the heavily cratered surface of Pallas, we explored its past collisional evolution, as well as that of the other two largest main-belt objects, Ceres and Vesta, through a series of Monte Carlo simulations (Methods). In each simulation, all collisional events capable of producing $D_c \geq 40$ km craters were recorded, using the π-scaling law[17] to relate the crater diameter to the size of the impactor. The output of the simulations are shown in Fig. 4: the derived synthetic crater density on Pallas, $(1.9 \pm 0.5) \times 10^{-4}\,\mathrm{km}^{-2}$ (3σ uncertainty), turns out to be about two and three times larger than on Ceres and Vesta, respectively. Our simulations therefore hint towards the existence of even more cratered units on Pallas that are not seen in the SPHERE images. The results of our simulations directly reflect the different collisional environments and bulk properties of the three objects, including their size, bulk density, intrinsic collisional probability and, most importantly, average impact speed: while Ceres and Vesta are on rather circular and low-inclination orbits, Pallas's large orbital eccentricity ($e = 0.23$) and inclination ($i = 34.8°$) imply typical impact velocities of ~$11.5\,\mathrm{km\,s}^{-1}$ with other main-belt asteroids, versus ~5.1 and $5.3\,\mathrm{km\,s}^{-1}$ for the other two bodies, respectively. Such large impact velocities of course drastically increase the number of projectiles able to create large craters owing to the steep size frequency distribution of the asteroid belt (slope approximately −2.5 in this size range[18]). Specifically, the minimum impactor size needed to produce a $D_c \geq 40$ km size crater on Pallas is ~2.4 km, whereas it is ~3.8 and ~4.3 km for the other two objects, respectively, implying a pool of three to four times more impactors for Pallas. This is only partially compensated by the lower intrinsic collisional probability between Pallas and impactors originating from the asteroid main belt. The heavily cratered surface of Pallas therefore appears to be a natural outcome of its peculiar orbit.

Next, the deconvolved images were fed into the All-Data Asteroid Modeling (ADAM) algorithm[19] together with previously acquired adaptive optics images from the Keck observatory (Supplementary Table 2) and optical light curves (Supplementary Table 3) to precisely retrieve Pallas's spin orientation and three-dimensional shape (Methods). Direct comparison between the SPHERE images and projections of the resulting model are shown in Fig. 2. The model has a volume-equivalent diameter of $D = 513 \pm 6$ km. Semi-axes along the principal axes of inertia $(284 \times 266 \times 224) \pm 6$ km indicate substantial departure from hydrostatic equilibrium considering Pallas's current rotation period of 7.8 h (Methods and Supplementary Fig. 2). This deviation can be explained by a substantial flattening of the south pole of Pallas (Supplementary Fig. 3) that could relate to the existence of an ancient impact basin, similar to Rheasilvia on Vesta, and by a change of its rotation period, from ~6.2 h to 7.8 h, during such a basin-forming impact. The south pole basin would represent 6 ± 1% of the current volume of Pallas, which is much larger than the volume of Rheasilvia (~3 ± 1% of the total volume of Vesta[20]). Another large excavation, roughly 1% the volume of Pallas, is found near its equator (Fig. 2). Using a smoothed particle hydrodynamics (SPH) code to model the formation of the basins and their ejected fragments, we found that the size and volume of the equatorial basin are best reproduced assuming a large oblique impact with a 60–90-km-sized projectile (Methods). Simulations of the subsequent orbital and collisional evolution of the resulting fragment population align well with both the orbital distribution and the size frequency distribution (SFD) of the current Pallas family after $1.7^{+0.2}_{-0.4}$ billion years (Gyr) of evolution. This implies the equatorial basin could very well be the remnant of the Pallas family-forming event. Similar simulations for the south pole basin, on the other hand, suggest that it does not relate to the present-day family.

Combining the volume measured from our three-dimensional shape model with available mass estimates (average value $(2.04 \pm 0.03) \times 10^{20}$ kg; Methods, Supplementary Fig. 4 and Supplementary Table 4) yields a density of $2.89 \pm 0.08\,\mathrm{g\,cm}^{-3}$ (1σ uncertainty), notably different from that of both Ceres ($2.16 \pm 0.01\,\mathrm{g\,cm}^{-3}$)[2] and Vesta ($3.46 \pm 0.03\,\mathrm{g\,cm}^{-3}$)[4], suggesting a distinct bulk composition for Pallas. In particular, Pallas's higher density with respect to Ceres is most likely explained by a lower internal water-to-rock fraction, which is also consistent with Pallas's higher and seemingly more stable topography. Further, assuming an interior with little porosity, Pallas's density is fully compatible with the average grain density of CM chondrite meteorites ($2.90 \pm 0.08\,\mathrm{g\,cm}^{-3}$)[21], Pallas's closest spectral analogues in the 3 μm spectral region[6]. This opens the possibility that Pallas accreted from the same starting material as the CM-like Ch- and Cgh-type asteroids[22]. In this scenario, spectral differences between these bodies over the visible and near-infrared wavelengths would result from distinct subsequent thermal and impact evolutions, owing to the larger size of Pallas and its unique collisional environment (see additional discussion in Methods).

A similar formation time for Pallas and the CM chondrites (3–4 million years (Myr) after the formation of calcium–aluminium-rich inclusions (CAIs))[23] would imply that the interior of Pallas never reached the silicate dehydration temperature (~820 K) necessary to trigger the differentiation of a denser silicate core below a hydrated mantle, implying it has a rather homogeneous interior (Methods and Supplementary Fig. 5). However, given Pallas's large size, partial differentiation (that is, separation of water from silicates and upward flow) must have occurred in its interior, leading to an enrichment in salts that could explain Pallas's high albedo ($p_v = 12$–17%)[7,8] with respect to Ch-/Cgh-type asteroids ($p_v = 6 \pm 2\%$)[24]. The presence of a bright spot with ~10% brightness enhancement on Pallas (Fig. 1), reminiscent of those found on Ceres[25], may provide additional support for the existence of salt deposits on its surface. However, alternative origins, such as the accretion of a bright exogenic material (for example, ordinary chondrite) or the presence of unresolved ejecta blanket of a fresh impact that excavated bright material from the subsurface, cannot at present be ruled out. Considering that some studies proposed that the near-Earth object Phaethon originated from Pallas[26,27] (see discussion in Methods), we hypothesize that the presence of salts (therefore, sodium) in Pallas is at the origin of the unusual diversity of sodium content measured in the Geminid meteor stream[28–32] emitted by Phaethon[33].

Methods

Cratering on Pallas. Pallas exhibits numerous large ($D_c > 30$ km) impact features, including various complex craters showing evidence for a central peak (Supplementary Fig. 1). The nearly pole-on orientation of the asteroid during our 11 sets of SPHERE observations—6 for the southern hemisphere and 5 for the

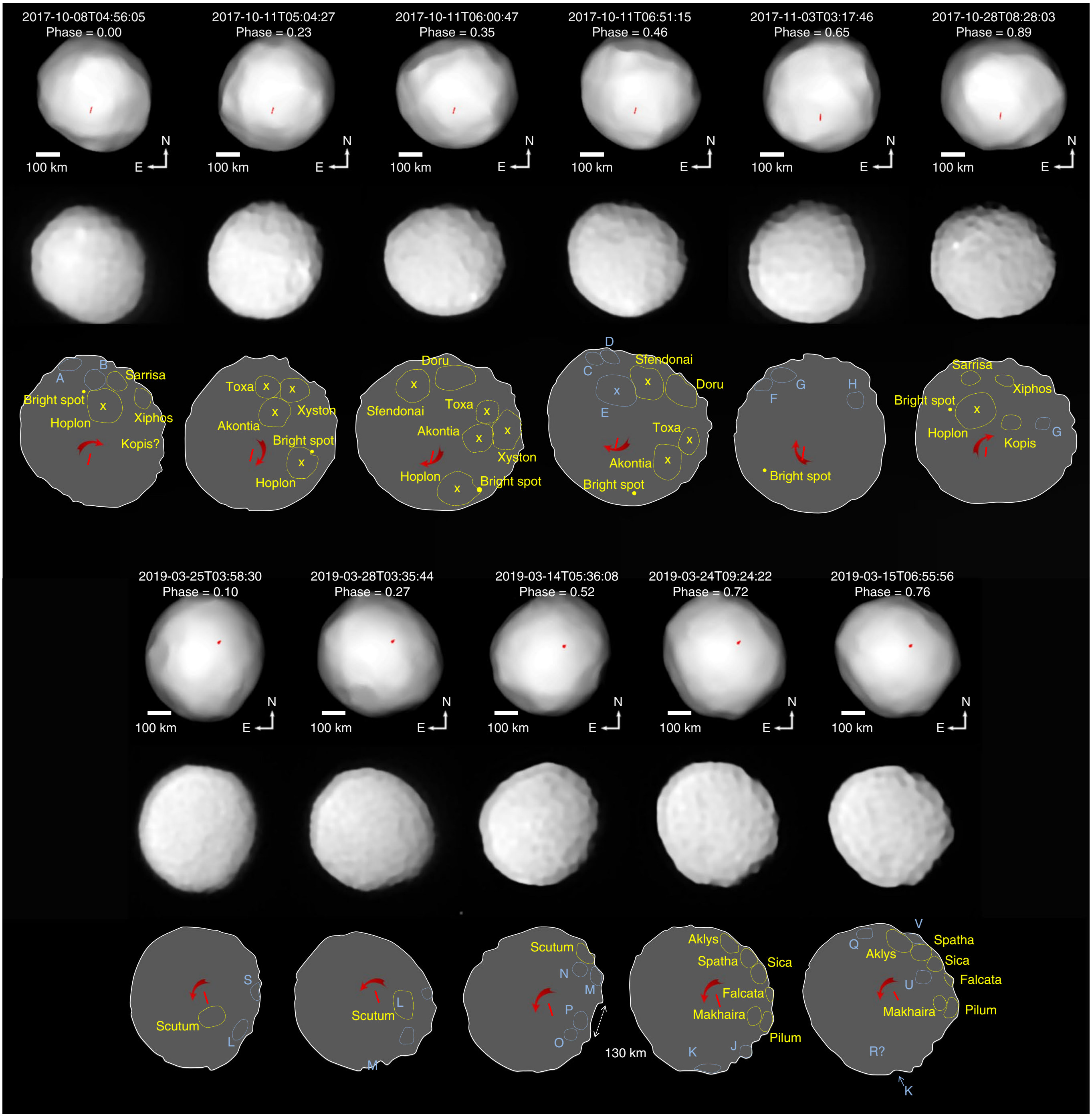

Fig. 2 | Deconvolved images of (2) Pallas, compared with projections of the ADAM shape model and sketches highlighting the main geological features identified on Pallas. The top three rows correspond to the southern hemisphere and the bottom three rows correspond to the northern hemisphere. Features detected at a single epoch are shown in blue and designated by uppercase letters. Features tracked throughout multiple rotation phase angles are in yellow and named after ancient Greek names of weapons (asteroid Pallas being named after Pallas Athena, the Greek goddess of war; Supplementary Table 1). The x marks indicate the locations of detected central peaks in complex craters (Supplementary Fig. 1). The epochs are ordered by increasing rotation phase. The red segment indicates Pallas's spin axis.

northern one—allowed accurate identification of the craters on both hemispheres throughout a complete rotational phase period.

We first removed the brightness gradient from each SPHERE image, which depends on the local illumination (local incidence, reflection and phase angle), following the method outlined in Fétick et al.[13]. The craters were then visually searched on the images, simultaneously using a projection of the ADAM shape model to measure their planetocentric coordinates. Owing to imperfect adaptive optics corrections and deconvolution of the images, many features that could be interpreted as craters might actually be artefacts and/or correlated noise in the images. To avoid false positives, each series of observation was carefully examined, and only features consistently present across a full set of images were recorded. Specifically, each sequence of SPHERE observations consisted of five images being simultaneously recorded by the two ZIMPOL cameras[9], resulting in a total set of ten images per observing epoch. Confirmed craters are those found throughout at least one complete sequence of ten images.

We then measured the crater diameter by extracting their brightness profile on the image. We defined the crater edge as the location where the profile inflects symmetrically on both sides of the centre of the crater. Diameters were estimated

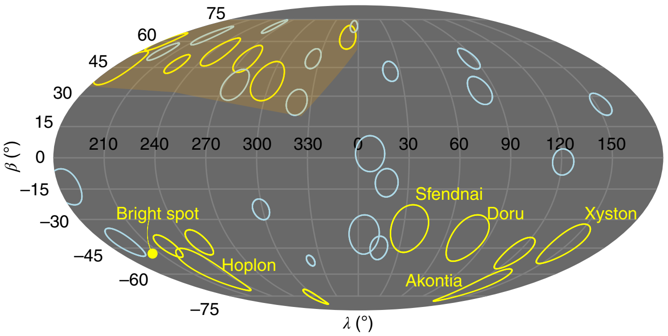

Fig. 3 | Mollweide projection of the 36 craters and the bright spot identified on the surface of Pallas. The same colour code as in Fig. 2 is used for the craters. The highly cratered region is highlighted in light orange. The names of the five largest craters are indicated.

as the distance between the two opposite ends of the edge, orthogonally to the direction of the subsolar point to account for the viewing angle. For those craters that are visible at multiple epochs of observation, we checked the consistency of our method by comparing values computed from the different epochs.

Using this method, a total of 36 craters were identified on Pallas, including 34 with diameter $D_c \geq 40$ km (Supplementary Table 1). Considering our careful rejection of possible false positives, which probably led to the rejection of a few true features, this number should be considered as a lower limit. In addition, several craters located near the subsolar point, where shadowing was minimal, might have been also missed. Anyhow, using our volume-equivalent diameter of $D = 513$ km, the number of 34 craters translates to an observed average number density of $N\,(D_c \geq 40\,\text{km}) = 4.1\times10^{-5}$–$5.5\times10^{-5}\,\text{km}^{-2}$, that is, more than twice larger than the average crater density on Vesta in this size range[34]. The interval of values provided here reflects the uncertainty on the surface of Pallas properly sampled by SPHERE: while the full surface was covered, the equatorial region was seen almost edge-on owing to the nearly pole-on orientation of Pallas during our observations. This probably explains the apparent lack of craters located between planetocentric latitudes of −15 and +15° (Fig. 3). For this region representing ~25% of the total surface of Pallas, we assumed that between 75 and 100% of the surface was accurately covered by our observations, and propagated this assumption to the uncertainty on crater density. Global crater frequency measurements, however, do not make a lot of sense, because they average crater counts over multiple geological units with different ages. The most heavily cratered area of Pallas is found in the northwest region, between approximately planetocentric longitude $\lambda = 180$–$0°$, and latitude $\beta = 35$–$75°$ (Fig. 3). This region represents an area of 7.2×10^4 to $9.3\times10^4\,\text{km}^2$ and contains 13 craters larger than 40 km in diameter (14 larger than 30 km), implying a crater number density $N\,(D_c \geq 40\,\text{km}) = (1.6\pm0.2)\times10^{-4}\,\text{km}^{-2}$. This is comparable to the oldest and most heavily cratered terrains found on Ceres and Vesta, such as the cratered terrain of Ceres's Ezinu quadrangle, with $N\,(D_c \geq 45\,\text{km}) = 1.4\times10^{-4}\,\text{km}^{-2}$ (ref. [14]), and the north pole of Vesta, with $N\,(D_c \geq 40\,\text{km}) = 1.5\times10^{-4}\,\text{km}^{-2}$ (ref. [15]). The vast majority of geological units on Ceres and Vesta are far less cratered[14–16,35–37].

Modelled cratering record. To understand the origin of the heavily cratered surface of Pallas, we explored its 4-Gyr-long collisional evolution, as well as that of Ceres and Vesta, through series of Monte Carlo simulations performed with the Boulder code[38,39]. The expected crater density on the three objects was evaluated by extracting all relevant collisional events in an extended set of 100 simulations per object. Specifically, using the π-scaling[17] for the relation $D_c(d_p)$ between the crater and projectile sizes, we recorded all events able to produce $D_c \geq 40$ km to allow a direct comparison between simulations and observations. The projectile size needed to create a given crater size and, therefore, the frequency of large collisions in our simulations highly depends on the choice of the scaling law[40]. However, the resulting relative differences between the three bodies (Ceres, Vesta and Pallas) is probably minor when using the same scaling law for all of them.

Collisional probabilities (P_i) and impact velocities (v_{imp}) were calculated from the observed orbital distribution of the main belt, and an evolving SFD providing the best match to the observed SFD after 4-Gyr evolution. Relevant input parameters of our simulations were calculated from the current osculating orbital elements of the asteroids and are summarized in Supplementary Table 5. Using proper orbital elements instead of the osculating ones does not change significantly the value of the derived parameters. For instance, in the case of Pallas, we derived $P_i = 2.17\times10^{-18}\,\text{km}^{-2}\,\text{yr}^{-1}$ and $v_{\text{imp}} = 11.49\,\text{km}\,\text{s}^{-1}$ when using current elements ($e = 0.23$, $i = 34.8°$), and $P_i = 1.89\times10^{-18}\,\text{km}^{-2}\,\text{yr}^{-1}$ and $v_{\text{imp}} = 11.25\,\text{km}\,\text{s}^{-1}$ for proper elements ($e = 0.28$, $i = 33.2°$), implying a variation of ~10% and ~2%, respectively. The resulting synthetic crater densities for Ceres, Vesta and Pallas are as follows: $(1.0\pm0.3)\times10^{-4}\,\text{km}^{-2}$, $(0.6\pm0.3)\times10^{-4}\,\text{km}^{-2}$ and $(1.9\pm0.5)\times10^{-4}\,\text{km}^{-2}$, respectively (Fig. 4). Here, the range of values reflect the Poisson uncertainty due to the stochasticity of the collisional process.

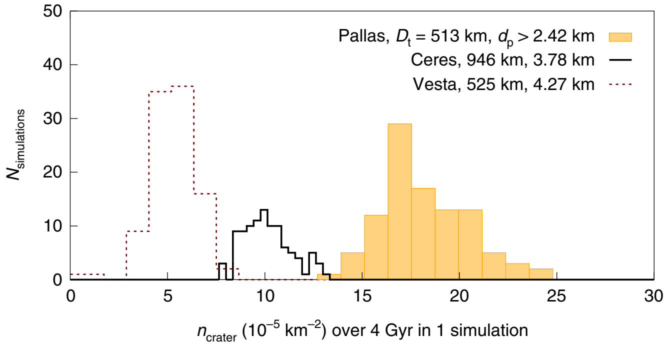

Fig. 4 | *N*-body simulations link the heavily cratered surface of Pallas to its highly inclined and eccentric orbit inducing a high average impact speed on this body. The histograms show the number of collisional events per surface unit able to create a crater with $D_c \geq 40$ km for each of the three largest asteroids: (1) Ceres, (4) Vesta and (2) Pallas. A total of 100 Monte Carlo simulations were run for each object. The target size D_t and the projectile diameter d_p needed to create the craters are provided in the legend. The high impact rate per surface unit on Pallas reflects its large median impact velocity of $v_{\text{imp}} = 11.5\,\text{km}\,\text{s}^{-1}$, compared with the typical velocity of ~5.8 km s^{-1} for the main belt.

The derived estimates directly relate to the different collisional environment of the three objects. In particular, Pallas is located in a more violent environment due to its eccentric ($e = 0.23$) and highly inclined ($i = 34.8°$) orbit that implies substantially larger impact velocities v_{imp}. This, of course, increases the number of available projectiles, because d_p needed to create $D_c \geq 40$ km is smaller, and the SFD of the asteroid belt is steep (slope −2.5 in this size range[18]). This is only partially compensated by the lower intrinsic probability of collisions between Pallas and impactors from the asteroid belt. Ceres is about twice larger than the other two bodies but gravitational focussing, expressed as $f_g = 1 + (v_{\text{esc}}/v_{\text{imp}})^2 \doteq 1.01$, where v_{esc} is the escape velocity and v_{imp} the impact velocity, does not contribute substantially.

Three-dimensional shape reconstruction. We used the ADAM inversion procedure[19,41–44] to reconstruct the shape and spin of Pallas, using as input the complete set of disk-resolved images and optical light curves listed in Supplementary Tables 2 and 3, respectively, and occultation data described in Hanuš et al.[44] for sanity checks. Our set of images comprises both our VLT/SPHERE observations, as well as Keck/Second Generation Near Infrared Camera (NIRC2)[45] images retrieved from the Keck Observatory Archive. While the NIRC2 images have a lower angular resolution than the SPHERE ones, these images sample additional observing geometries of Pallas that are complementary to our own dataset for shape reconstruction. We first created a low-resolution shape model using the spherical harmonics parameterization and our complete dataset of images and light curves as input. Owing to the disparity in imaging resolution of the Keck/NIRC2 and VLT/SPHERE images, we then constructed a higher resolution model from the SPHERE data only, using the low-resolution shape model as initial input. Finally, we allowed the vertices to move independently of parameterization, subject only to the regularization and adaptive optics data fit functions.

Overall, our model fits the image boundaries at the subpixel level and recovers most of the high-resolution features present in the SPHERE images (Fig. 2). The best triaxial ellipsoid fit to the three-dimensional shape model has a volume-equivalent diameter of $D = 513\pm6$ km, with semi-axes along the principal axes of inertia $(284\times266\times224)\pm6$ km. An equator-on projection of the model reveals that the south pole is substantially flattened (Supplementary Fig. 3), which could relate to the existence of a large basin, possibly created by a single or a few substantial impacts, like Rheasilvia on Vesta[20]. This feature is unseen on the SPHERE images, due to the nearly pole-on orientation of the asteroid during the observations, and could only be retrieved due to the three-dimensional shape reconstruction and the use of complementary light curves. The basin would represent ~6 ± 1% of the current volume of Pallas. Its polar location is consistent with reorientation of the rotation axis towards maximum moment of inertia, which occurs over timescales of the order of ~10^5 yr for a Pallas-size body[46].

The fossile shape of Pallas. Our ADAM shape model was further used to investigate the hydrostatic shape of (2) Pallas, assuming both a homogeneous and a two-layer differentiated interior. The hydrostatic equilibrium figure of a homogeneous body can be calculated using the MacLaurin equation, whereas for a differentiated body it needs to be solved numerically. Here, we used a numerical integration of the Clairaut's equations developed to an order that depends on the geodetic parameter m (refs. [47,48]) that is a function of the angular spin velocity and mean density of the body. Depending on the value of that parameter and the accuracy of available observations, the Clairaut's equations may be developed to first, second or third order[49]. This method has been previously applied to the hydrostatic figures of Earth[47] and Ceres[2,48].

Supplementary Fig. 2 compares the (a–c) dimension of Pallas with respect to a similar-size body at equilibrium, where a and c are the equatorial and polar radii of the object. The shape of Pallas substantially deviates from equilibrium considering its current rotation period (~7.8 h), implying it was substantially reshaped by a large impact and/or that it used to rotate faster in the past. We investigated whether the putative south pole basin could account for this deviation. To do so, a best-fit ellipsoid was adjusted to the three-dimensional shape model of Pallas, excluding the south pole (specifically, meshes below −31° latitude were rejected from the fit; Supplementary Fig. 3). The resulting ellipsoid has semi-major axis 282 × 262 × 249 km, which is closer to a hydrostatic shape, but still requires a change of rotation period of 1.6 h, down to ~6.2 h, to be at equilibrium.

For a homogeneous sphere, the change in angular momentum is given by $\Delta L = 2/5MR^2 2\pi/|P - P'|$, where M is the mass, R the radius and P the rotation period. If we simply assume $\Delta L = m_{\mathrm{p}} v_{\mathrm{imp}} \sin(45°) R$, where subscript p refers to 'projectile', and express $d_{\mathrm{p}} = 2 \times [3m_{\mathrm{p}}/(4\pi\rho_{\mathrm{p}})]^{1/3}$, then the projectile size needed for $|P - P'| = 1.6$ h is $d_{\mathrm{p}} \approx 48$ km assuming $\rho_{\mathrm{p}} = 3{,}000\,\mathrm{kg\,m^{-3}}$ and $v_{\mathrm{imp}} = 11.5\,\mathrm{km\,s^{-1}}$. This translates to a crater size of ~370 km according to the π-scaling law[17], that is, ~70% of the current size of Pallas, which could represent the south pole basin. Therefore, it seems very plausible that the fitted ellipsoid in Supplementary Fig. 3 represents the original, pre-impact shape of Pallas.

The present-day Pallas family. Pallas is surrounded by a few hundred small ($D < 20$ km) bodies that together form a distinct asteroid family[50]. We describe here the method we used to identify the family members, whose orbital properties were subsequently used to examine the physical conditions of the family-forming event.

The Pallas family is well-defined and taxonomically homogeneous. It is located at high inclination, where few background asteroids exist. The geometric albedo of the family members is comprised in the range $p_v \in (0.06; 0.24)$[51], and colours from the Sloan Digital Sky Survey (SDSS)[52] are such that the colour index $a\star < 0$ mag. The dynamic environment of Pallas is complex and affected by several mean-motion and secular resonances. As a consequence, many asteroids are on chaotic, unstable or resonant orbits, with proper orbital elements that can quickly shift in eccentricity and/or inclination. Because of this, many family members can be missed when identifying them using proper elements. We therefore instead chose to consider the averaged mean orbital elements of the asteroids, including all forced terms. The mean elements were calculated carefully to avoid aliasing of fast orbital frequencies, with a four-stage convolution filter based on the Kaiser windows[53]. Input sampling of the osculating elements was set to 1 yr and we used four filters denoted A, A, A, B with decimation factors of 10, 10, 5, 3, resulting in output sampling of the mean elements of 1,500 yr. Finally, we applied a running-average filter with a window of 1 Myr and output sampling of 0.1 Myr. Using this method, we were able to use all of the observed multi-opposition asteroids, not only those with stable proper elements (473 versus 319 bodies). We used exactly the same algorithm for our synthetic families generated for investigating the orbital evolution of the Pallas family through N-body simulations (see below), allowing a direct comparison of our simulations with observations. Supplementary Fig. 6 displays the mean orbital elements of the observed population of the family members, interlopers and background asteroids in the vicinity of Pallas.

Orbital evolution of the family. The long-term orbital evolution of the Pallas family was studied by use of the symplectic N-body integrator SWIFT-Rmvs3[54] to estimate the age of the family. We explored the simplest case in which the current family was created in a single, large collision. More complicated scenarios, for example, in which the family was subsequently rejuvenated by smaller impacts, are beyond the scope of this work. Our dynamical model[55] included the outer Solar System planets, and a barycentric correction to account for the inner planets. Pallas was treated as a massive body, as close encounters can enhance diffusion in its vicinity. Our code further included the Yarkovsky diurnal and seasonal effects[56,57], the Yarkovsky–O'Keefe–Radzievskii–Paddack (YORP) effect[58], and reorientation or reshaping during random collisions and when bodies reach a critical spin rate. The time step was set to $\Delta t = 36.525$ d, and the time spanned up to 4 Gyr.

We created a synthetic family of 1,380 bodies with assumed isotropic velocities[59] and spins, escape velocity $v_{\mathrm{esc}} = 324\,\mathrm{m\,s^{-1}}$, and maximum velocity difference $v_{\max} = 600\,\mathrm{m\,s^{-1}}$. We derived the preferred true anomaly $f = 140°$ and argument of perihelion $\omega = 60$ at the time of impact, using the Gauss equations to fit ellipses to the distribution of the Pallas family in the a_{m} versus e_{m} and a_{m} versus $\sin I_{\mathrm{m}}$ spaces of the mean orbital elements, where a_{m}, e_{m} and I_{m} are the mean semi-major axis, mean orbital eccentricity and mean orbital inclination, respectively.

Thermal parameters of our model included the bulk density $\rho = 2{,}890\,\mathrm{kg\,m^{-3}}$, the density of surface layers (regolith) $\rho_{\mathrm{surf}} = 1{,}500\,\mathrm{kg\,m^{-3}}$, the heat capacity $C = 680\,\mathrm{J\,kg^{-1}\,K^{-1}}$, the thermal conductivity $K = 10^{-3}\,\mathrm{W\,m^{-1}\,K^{-1}}$, the Bond albedo $A = 0.10$ and the infrared emissivity $\epsilon = 0.9$. When unknown, diameters D were calculated from absolute magnitudes H assuming the median value of geometric albedo of the Pallas family members $p_{\mathrm{v}} = 0.122$ (ref. [60]).

To compare our N-body integration with the observed family, we used the method of Brož and Morbidelli[61], which consists of rescaling the synthetic population to match the observed SFD, and then computing the χ^2 for the number of objects counted in boxes defined in the (a_{m}, e_{m}) space (Supplementary Fig. 7). The evolution of the $\chi^2(t)$ throughout our integration is shown in Supplementary Fig. 8. It decreases from the initial value $\chi^2/N_{\mathrm{box}} \simeq 3.6$ down to 1.35, with the best-fit value corresponding to $t = 1.68$ Gyr. The uncertainty on the age was computed from the scatter of the $\chi^2(t)$ values due to the random selection procedure, assuming the best-fit value is acceptable. By doing so, we derived an estimate of the family's age of $t = 1.3$–1.9 Gyr.

As a by-product, we calculated the exponential decay timescales for bodies of various sizes, which are necessary inputs for Monte Carlo collisional models (see below). The values are $\tau = 374$, 419, 782, 1,390, 2,050, and 2,130 Myr for the size bins between $D = 0.5$, 1, 2, 5, 10, 20, 30 km, respectively.

The family-forming impact. We then performed combined SPH/N-body simulations[62–64] aiming at deriving the impact parameters providing the best fit to the orbital distribution and SFD of the Pallas family members, and allowing a direct comparison of the resulting impact features with observations. Here, again, we assumed that the Pallas family originated from a single, large collision. While multiple small events may eject enough material to produce the present-day family, a large impact is needed to account for the size of the largest observed fragment ($D_{\mathrm{lf}} \sim 20$ km). In addition, fragments produced in a cratering event are usually smaller than the projectile, and kilometre-size fragments are continuously removed from the family by Yarkovsky drift[56,57] and chaotic diffusion over timescales of a few hundred million years, implying they cannot accumulate over 4 Gyr. Consequently, our simulations, which are constrained by $D > 10$ km fragments, are not affected by small cratering events.

Our model included a fragmentation without gravity and gravitational reaccumulation[65]. We used Tillotson's equation of state[66], von Mises's yielding criterion[67] and Grady and Kipp's fracture model[68]. Initial conditions included two spherical bodies (the target and the projectile), with target size $D_{\mathrm{pb}} = 513$ km, and impact velocity $v_{\mathrm{imp}} = 12\,\mathrm{km\,s^{-1}}$. Our simulations covered a range of specific energy ratios $Q/Q^{\star}_{\mathrm{D}}$, where $Q^{\star}_{\mathrm{D}}$ denotes the strength from the scaling law, provided in Supplementary Table 6. We used an SPH discretization in space, with number of particles $N_{\mathrm{part}} \doteq 1.4 \times 10^5$, and a predictor–corrector discretization in time. The time step was limited by the Courant criterion, and to limit changes in energy, pressure and fracture damage per time step to accurately control the integrations as described in Benz and Asphaug[69]. Given the target size and v_{imp}, the chosen time span was 200 s. We used standard artificial viscosity parameters $\alpha_{\mathrm{av}} = 1.5$, $\beta_{\mathrm{av}} = 3.0$, and a modification of the scalar damage $\mathcal{D}$, as in Ševeček et al.[64]. Concerning the N-body part of the simulation, we used a handoff relation $R_{\mathrm{i}} = [3m_{\mathrm{i}}/(4\pi\rho_{\mathrm{i}})]^{1/3}$, a tree-code with the opening angle $\theta = 0.5$ rad, and a hexadecapole approximation for the gravity. We assumed a perfect merging. The time step was $\Delta t = 10^{-6}$ (in $G = 1$ unit), and the time span 50,000 Δt.

Our simulations covered a relevant range of outcomes, shown in Supplementary Fig. 9, from weakly catastrophic to large cratering events. In every simulation, the target was fully damaged. The velocity field at the end of the fragmentation phase indicates that the first three higher-energy impacts $Q/Q^{\star}_{\mathrm{D}} \geq 0.067$ affected essentially the whole surface of the target, while the last three produced a large crater and only partial modification of the surface.

We determined the excavated mass before fall-back as the sum of all particles located 30 km above the surface of the target, allowing for some expansion of the target. The simulations that better match the observed SFD of the family (rows 3 and 4 in Supplementary Table 6) have excavated mass $M_{\mathrm{ex}} = 0.016$ to 0.027 (in M_{pb} units), implying the equatorial excavation is more likely to be linked to the present-day Pallas family than the south pole basin. From Supplementary Fig. 9, we measured a transient crater size of at least 250 km, which can subsequently increase, possibly up to the target size, during relaxation of the surface. However, the crater may not be well preserved in the highest-energy impacts due to substantial reaccumulation.

Supplementary Fig. 10 shows the SFD of the fragments after reaccumulation, assuming their final density is the same as before the impact ($\rho_0 = 2.89\,\mathrm{g\,cm^{-3}}$). If we assume that the ejected fragments have retained their expanded densities, $\rho < \rho_0$, this would shift their SFD towards slightly larger D, possibly by a factor of 1.5. Consequently, lower-energy oblique impacts would produce a better fit to the observed SFD. Our simulations covered a reasonable range of $Q/Q^{\star}_{\mathrm{D}}$, so that the largest fragments have sizes $D_{\mathrm{lf}} = 14$–36 km that are relatively close to the observed value ($D_{\mathrm{lf}} = 22.46$ km). The synthetic SFDs have significantly steeper slope than the observed one (approximately −5.0 versus −2.2), which indicates substantial subsequent collisional and orbital evolution.

Next, the ejected mass was estimated as the sum of all fragments from the target. We did not include the projectile, which either vaporized or whose remaining fragments escaped the space of proper elements of the family. Ejected masses are comprised between 0.015 to 0.028 (M_{pb} units; Supplementary Table 6), which is comparable to M_{ex}.

Evolution of the SFD of the family. Independent constraints on the age of the family were derived using a Monte Carlo collisional model, using as input the synthetic SFDs derived from our SPH simulations for the initial family. This method simultaneously allows estimation of the probability that such a family is created over the course of evolution. We assumed constant intrinsic collisional probabilities $P_i = 2.86 \times 10^{-18}$, 2.17×10^{-18} and $2.87 \times 10^{-18}\,\mathrm{km}^{-2}\,\mathrm{yr}^{-1}$ for the three relevant combinations of collisions (MB–MB, MB–Pallas, Pallas–Pallas, where MB designates main-belt objects), and mutual impact velocities $v_{\mathrm{imp}} = 5.77$, 11.49 and 13.05 km s^{-1}, calculated according to Bottke and Greenberg[70]. Our model includes a size-dependent dynamical decay from Bottke et al.[71] for the main belt, and from our previous *N*-body simulation for the Pallas family.

A number of additional parameters were specified, including the scaling law $Q^*_{\mathrm{D}}(r)$, which was taken from Benz and Asphaug[72] for basalt material, with $\rho = 2.89\,\mathrm{g\,cm}^{-3}$, at the impact velocity 5 km s^{-1}. This is inconsistent with typical velocities on Pallas, but it cannot be easily improved unless a big matrix of simulations is computed. We also used a modification of the parametric relation for the mass of the largest fragment $M_{\mathrm{lf}}(Q/Q^*_{\mathrm{D}})$, which seems necessary for small cratering events. Initial conditions are quite close to the observed SFD, except for the synthetic family which is steeper (−5.0 cumulative). A discretization in mass is performed with a logarithmic factor 1.5. The output time step of the simulation was set to $\Delta t = 10$ Myr, and the nominal time spanned 4 Gyr. At least 10 Monte Carlo simulations were performed, because of fractional probabilities of large breakups and lower-probability events.

The results are summarized in Supplementary Fig. 11. A typical timescale of a significant (10%) evolution of the family's SFD is of the order of 100 Myr, mostly due to dynamical decay and secondary MB–Pallas collisions. After 2 Gyr of evolution, about a third of simulations produced synthetic families with $D > 22.46$ km for the largest fragment. We therefore consider the Pallas family to be a likely outcome of the equatorial excavation-forming event. The event responsible for the south pole basin, on the other hand, requires up to 3 to 4 Gyr of evolution owing to the steeper SFD of the collisional fragments. This longer time is in contradiction with the simulated orbital evolution of the family, implying that the south pole basin is unlikely to relate to the present-day Pallas family.

Present-day composition of Pallas. Combined with available mass estimates from the literature (Supplementary Table 4 and Supplementary Fig. 4), our three-dimensional shape model of Pallas returns a bulk density of $2.89 \pm 0.08\,\mathrm{g\,cm}^{-3}$, in perfect agreement with the grain density of CM chondrite meteorites ($2.90 \pm 0.08\,\mathrm{g\,cm}^{-3}$)[21] assuming near-zero porosity in the interior of Pallas. Whereas CM chondrites exhibit the same hydration signature in the 3 μm wavelength range as Pallas[6], these meteorites are usually linked to Ch-/Cgh-type asteroids[22,73,74] and have distinct spectral properties from Pallas in the visible and near-infrared (0.4–2.5 μm). Specifically, Pallas is bluer and brighter than most CM chondrites and it does not exhibit the 0.7–0.9 μm absorption features that is present in the meteorite spectra.

A direct link between Pallas and CM chondrites therefore does not appear obvious. It is possible, however, that Pallas and the parent bodies of CM chondrites accreted from the same initial material, as suggested by their similar densities, and that their spectral differences come from distinct subsequent thermal and collisional evolution owing to Pallas's large size and distinct collisional environment. In particular, frequent high-energy impacts and micro-meteorite bombardment on Pallas could have led to partial dehydration of its surface, which could explain its bluer and brighter spectrum and the lack of phyllosilicate signatures in the visible. On the other hand, the 3 μm signature would have been preserved because of its much deeper and broader profile. Along these lines, laboratory experiments have shown that artificially heated CM chondrites usually exhibit bluer, brighter (although not as bright as Pallas) and more featureless spectra[75,76]. Based on these considerations, it appears possible that Pallas represents the parent body of heated CM chondrites, for which no parent body has been identified so far.

Pallas's derived bulk density is further higher than Ceres's ($2.16 \pm 0.01\,\mathrm{g\,cm}^{-3}$)[2], suggesting a lower water-to-rock ratio, in agreement with its higher and seemingly more stable topography. A lower water content for Pallas with respect to Ceres is also in agreement with the survival of the Pallas family members over several hundred million years, while the lack of a Ceres family points towards rapid sublimation of impact fragments from Ceres[77].

Initial rock-to-ice ratio of Pallas. Assuming Pallas accreted from a mixture of anhydrous dust and ice, two distinct evolutionary pathways must be considered when assessing its early internal evolution. In the first scenario, Pallas accreted with about the same bulk water content as inferred from its measured density. This leads to a low water-to-rock ratio (W/R < 1) in the transient ocean generated by the decay of short-lived radioisotopes. In that case, Pallas did not differentiate, and its current surface would represent a collisionally evolved version of its original one. In the alternative case where Pallas's initial W/R was high (≫1), thermophysical modelling predicts the formation of an icy outer shell through the separation of water from the silicates, upward flowing and freezing towards the surface. This icy shell being missing at present implies that it would have been progressively removed by collisions exposing fresh ice and thus triggering their sublimation. In that scenario, the surface of Pallas today would represent the hydrated mantle of the proto-Pallas.

Considering that the measured density of Pallas is fully compatible with CM chondrites, as well as with its predicted mineralogy in the low W/R scenario studied by Castillo-Rogez et al.[78], which is also consistent with aqueous alteration conditions inferred for CM chondrites[79], we favour the low W/R scenario for its formation and evolution. Importantly, the modelled mineralogy includes small fractions of salts (for example, carbonates, chlorides), the presence of which could explain both the higher albedo of the Pallas family compared with other B-type asteroids[60,80], and albedo variations seen on the surface of Pallas.

Formation time and interior of Pallas. Whether Pallas's internal temperature reached the silicate dehydration threshold (~820 K) depends on its time of formation. One-dimensional thermal conduction was modelled using the approach developed by Castillo-Rogez et al.[81] and applied to a variety of bodies, including Pallas[82]. Specifically, heat was transferred by conduction with the following equation:

$$\frac{\partial(k(T)\partial(T)/r)}{\partial r} + \frac{2}{r}\left(k(T)\frac{\partial T(r)}{\partial r}\right) = \rho(r)C_{\mathrm{p}}(T)\frac{\mathrm{d}T(r)}{\mathrm{d}t} - H(r) \qquad (1)$$

where *T* is temperature (in Kelvin), *r* is local radius, *k* is thermal conductivity, *ρ* is material density, C_{p} is specific heat, *t* is time and *H* is internal heating (that is, radioisotope decay heat). Calculation of the radioisotope decay heat, the main heat source for Pallas, can be found in Supplementary Table 7. The properties of the materials used in the modelling are listed in Supplementary Table 8. Pure serpentine has a thermal conductivity of about 2.5 W m^{-1} K^{-1} while anhydrous silicates (olivine and pyroxene) have thermal conductivities up to 5 W m^{-1} K^{-1} (ref. [83]). The latter could be present if aqueous alteration was partial. Also, the presence of iron-rich compounds in the rock (such as iron sulfide and oxides) could increase the thermal conductivity further. In this study, we covered a range of thermal conductivities for the mantle from 0.5 to 2.5 W m^{-1} K^{-1} under the assumption that aqueous alteration might be advanced.

Using this model, we found that partial dehydration of the core of Pallas occurs for times of formation $T_0 < 2.5$ Myr after the formation of CAIs (Supplementary Fig. 5). Provided that the proposed association between CM chondrite meteorites and Pallas is correct, and considering the isotopic ages of CM chondrites (mostly >3.0 Myr after the formation of CAIs)[23], we conclude that the amount of radioisotopes accreted by Pallas was too low to trigger large-scale silicate dehydration and the differentiation of a denser silicate core below a hydrated mantle, thus implying a rather homogeneous interior. This finding is consistent with previous studies that found the primordial internal structure of CM parent bodies to be globally homogeneous[22,84–86]. However, considering Pallas's large size, early partial differentiation (water separation and upward flow) must have occurred in its interior and could explain the high albedo and its variations by an enrichment in salts through aqueous alteration.

The presence of salts in Pallas would further provide a natural explanation to the diversity of sodium contents measured in the Geminid meteor stream[28–32]. The Geminids are believed to originate from the 5−6 km Apollo-type asteroid (3200) Phaethon[33], a proposed fragment from the Pallas family that would have been emplaced in the near-Earth space following gravitational interactions with the Jovian mean-motion resonances[26,27]. The proposed link between Pallas and Phaethon, however, remains matter of debate: while the spectra of Phaethon, Pallas and the Pallas family members are strikingly similar in the visible and near-infrared, estimates of the albedo of Phaethon based on thermal measurements show some controversy: some values are consistent with those derived for Pallas and the Pallas family members[87–89], while others are much lower[90]. Polarimetric studies provide an independent insight into this controversy as the albedo of an asteroid can be evaluated from its maximum value of linear polarization degree P_{max} (ref. [91]) and/or from its polarimetric slope *h* (ref. [92,93]). High P_{max} values usually correspond to low albedos that are typical of C-type asteroids[91,94]. In case of Phaethon, however, the high value of P_{max} might be better explained by a large average regolith grain size and perhaps also a large surface porosity[91]. Albedo estimates derived from the polarimetric slope *h*, on the other hand, are less dependent on particle size. In the case of Phaethon, the albedo derived from the *h* value is intermediate (14 ± 4%)[95], in agreement with Pallas.

Finally, it should be noted that Phaethon does not exhibit the 3 μm absorption band that characterizes Pallas[96]. Whether this difference is due to the thermal evolution of Phaethon's surface (for example, the complete dehydration of surface minerals) in the near-Earth space, or to the fact that Phaethon is not genetically linked to Pallas, remains an open question that should be addressed by the future DESTINY+ fly-by mission to Phaethon[97] or by acquiring high-quality mid-infrared spectra of both Pallas and Phaethon with the James Webb Space telescope[98].

Data availability

As soon as papers for our large programme are accepted for publication, we will make the corresponding reduced and deconvolved adaptive optics images and three-dimensional shape models publicly available at http://observations.lam.fr/astero/.

Code availability

The code used to generate the three-dimensional shape is available at https://github.com/matvii/ADAM. The modified SWIFT integrator used to model the orbital evolution of the Pallas family is available at http://sirrah.troja.mff.cuni.cz/mira/mp/.

Received: 27 June 2019; Accepted: 19 December 2019;

References

1. Schmidt, B. E. et al. The shape and surface variation of 2 Pallas from the Hubble Space Telescope. *Science* **326**, 275–278 (2009).
2. Park, R. S. et al. A partially differentiated interior for (1) Ceres deduced from its gravity field and shape. *Nature* **537**, 515–517 (2016).
3. Carry, B. et al. Physical properties of (2) Pallas. *Icarus* **205**, 460–472 (2010).
4. Russell, C. T. et al. Dawn at Vesta: testing the protoplanetary paradigm. *Science* **336**, 684–686 (2012).
5. Beuzit, J. L. et al. SPHERE: the exoplanet imager for the Very Large Telescope. *Astron. Astrophys.* **631**, A155 (2019).
6. Larson, H. P., Feierberg, M. A. & Lebofsky, L. A. The composition of asteroid 2 Pallas and its relation to primitive meteorites. *Icarus* **56**, 398–408 (1983).
7. Tedesco, E. F., Noah, P. V., Noah, M. & Price, S. D. The supplemental IRAS minor planet survey. *Astron. J.* **123**, 1056–1085 (2002).
8. Alí-Lagoa, V., Müller, T. G., Usui, F. & Hasegawa, S. The AKARI IRC asteroid flux catalogue: updated diameters and albedos. *Astron. Astrophys.* **612**, A85 (2018).
9. Thalmann, C. et al. SPHERE ZIMPOL: overview and performance simulation. *Proc. SPIE* **7014**, 70143F (2008).
10. Vernazza, P. et al. The impact crater at the origin of the Julia family detected with VLT/SPHERE? *Astron. Astrophys.* **618**, A154 (2018).
11. Fusco, T. et al. Deconvolution of astronomical images obtained from ground-based telescopes with adaptive optics. *Proc. SPIE* **4839**, 1065–1075 (2003).
12. Mugnier, L. M., Fusco, T. & Conan, J.-M. MISTRAL: a myopic edge-preserving image restoration method, with application to astronomical adaptive-optics-corrected long-exposure images. *J. Opt. Soc. Am. A* **21**, 1841–1854 (2004).
13. Fétick, R. J. et al. Closing the gap between Earth-based and interplanet. mission observations: Vesta seen by VLT/SPHERE. *Astron. Astrophys.* **623**, A6 (2019).
14. Scully, J. E. C. et al. Ceres' Ezinu quadrangle: a heavily cratered region with evidence for localized subsurface water ice and the context of Occator crater. *Icarus* **316**, 46–62 (2018).
15. Schmedemann, N. et al. The cratering record, chronology and surface ages of (4) Vesta in comparison to smaller asteroids and the ages of HED meteorites. *Planet. Space Sci.* **103**, 104–130 (2014).
16. Hiesinger, H. et al. Cratering on Ceres: implications for its crust and evolution. *Science* **353**, aaf4759 (2016).
17. Melosh, H. J. *Impact Cratering: A Geologic Process* (Oxford Univ. Press,1989).
18. Gladman, B. J. et al. On the asteroid belt's orbital and size distribution. *Icarus* **202**, 104–118 (2009).
19. Viikinkoski, M., Kaasalainen, M. & Durech, J. ADAM: a general method for using various data types in asteroid reconstruction. *Astron. Astrophys.* **576**, A8 (2015).
20. Schenk, P. et al. The geologically recent giant impact basins at Vesta's south pole. *Science* **336**, 694–697 (2012).
21. Consolmagno, G., Britt, D. & Macke, R. The significance of meteorite density and porosity. *Chem. Erde Geochem.* **68**, 1–29 (2008).
22. Vernazza, P. et al. Compositional homogeneity of CM parent bodies. *Astron. J.* **152**, 54 (2016).
23. Doyle, P. M. et al. Early aqueous activity on the ordinary and carbonaceous chondrite parent bodies recorded by fayalite. *Nat. Commun.* **6**, 7444 (2015).
24. Masiero, J. R. et al. Preliminary analysis of WISE/NEOWISE 3-band cryogenic and post-cryogenic observations of main belt asteroids. *Astrophys. J.* **759**, L8 (2012).
25. Nathues, A. et al. Sublimation in bright spots on (1) Ceres. *Nature* **528**, 237–240 (2015).
26. de León, J., Campins, H., Tsiganis, K., Morbidelli, A. & Licandro, J. Origin of the near-earth asteroid Phaethon and the Geminids meteor shower. *Astron. Astrophys.* **513**, A26 (2010).
27. Todorović, N. The dynamical connection between Phaethon and Pallas. *Mon. Not. R. Astron. Soc.* **475**, 601–604 (2018).
28. Trigo-Rodríguez, J. M., Llorca, J., Borovička, J. & Fabregat, J. Spectroscopy of a Geminid fireball: its similarity to cometary meteoroids and the nature of its parent body. *Earth Moon Planets* **95**, 375–387 (2004).
29. Borovička, J., Koten, P., Spurný, P., Boček, J. & Štork, R. A survey of meteor spectra and orbits: evidence for three populations of Na-free meteoroids. *Icarus* **174**, 15–30 (2005).
30. Borovička, J. Spectroscopic analysis of Geminid meteors. In *Proc. 26th International Meteor Conference Bareges, France, 2007* (eds Rendtel, J. & Vaubaillon, J.) 42–51 (International Meteor Organization, 2010).
31. Kasuga, T., Watanabe, J. & Ebizuka, N. A 2004 Geminid meteor spectrum in the visible-ultraviolet region. Extreme Na depletion? *Astron. Astrophys.* **438**, L17–L20 (2005).
32. Kasuga, T. Thermal evolution of the Phaethon-Geminid stream complex. *Earth Moon Planets* **105**, 321–326 (2009).
33. Whipple, F. L. 1983 TB and the Geminid meteors. *IAU Circular* 3881 (1983).
34. Liu, Z. et al. A global database and statistical analyses of (4) Vesta craters. *Icarus* **311**, 242–257 (2018).
35. Marchi, S. et al. The violent collisional history of asteroid 4 Vesta. *Science* **336**, 690–694 (2012).
36. Marchi, S. et al. The missing large impact craters on Ceres. *Nat. Commun.* **7**, 12257 (2016).
37. Pasckert, J. H. et al. Geologic mapping of the Ac-2 Coniraya quadrangle of Ceres from NASA's Dawn mission: implications for a heterogeneously composed crust. *Icarus* **316**, 28–45 (2018).
38. Morbidelli, A., Bottke, W. F., Nesvorný, D. & Levison, H. F. Asteroids were born big. *Icarus* **204**, 558–573 (2009).
39. Cibulková, H., Brož, M. & Benavidez, P. G. A six-part collisional model of the main asteroid belt. *Icarus* **241**, 358–372 (2014).
40. Werner, S. C. & Ivanov, B. A. in *Treatise on Geophysics* (ed. Schubert, G.) 2nd edn 327–365 (Elsevier, 2015).
41. Viikinkoski, M. et al. VLT/SPHERE- and ALMA-based shape reconstruction of asteroid (3) Juno. *Astron. Astrophys.* **581**, L3 (2015).
42. Viikinkoski, M. *Shape Reconstruction from Generalized Projections*. PhD thesis, Tampere Univ. Technology (2016).
43. Marsset, M. et al. 3D shape of asteroid (6) Hebe from VLT/SPHERE imaging: implications for the origin of ordinary H chondrites. *Astron. Astrophys.* **604**, A64 (2017).
44. Hanuš, J., Marchis, F., Viikinkoski, M., Yang, B. & Kaasalainen, M. Shape model of asteroid (130) Elektra from optical photometry and disk-resolved images from VLT/SPHERE and Nirc2/Keck. *Astron. Astrophys.* **599**, A36 (2017).
45. McLean, I. S. & Chaffee, F. H. Instrumentation for the Keck Observatory. *Proc. SPIE* **4008**, 2–7 (2000).
46. Burns, J. A. & Safronov, V. S. Asteroid nutation angles. *Mon. Not. R. Astron. Soc.* **165**, 403–411 (1973).
47. Chambat, F., Ricard, Y. & Valette, B. Flattening of the Earth: further from hydrostaticity than previously estimated. *Geophys. J. Int.* **183**, 727–732 (2010).
48. Rambaux, N., Chambat, F. & Castillo-Rogez, J. C. Third-order development of shape, gravity, and moment of inertia for highly flattened celestial bodies. Application to Ceres. *Astron. Astrophys.* **584**, A127 (2015).
49. Lanzano, P. The equilibrium of a rotating body of arbitrary density. *Astrophys. Space Sci.* **29**, 161–178 (1974).
50. Nesvorný, D., Brož, M. & Carruba, V. in *Asteroids IV* (eds Michel, P. et al.) 297–321 (Univ. Arizona Press, 2015).
51. Mainzer, A. et al. *NEOWISE Diameters and Albedos V2.0* (NASA Planetary Data System, 2019); https://sbn.psi.edu/pds/resource/neowisediam.html
52. Ivezić, Ž. et al. Color confirmation of asteroid families. *Astron. J.* **124**, 2943–2948 (2002).
53. Quinn, T. R., Tremaine, S. & Duncan, M. A three million year integration of the Earth's orbit. *Astron. J.* **101**, 2287–2305 (1991).
54. Levison, H. F. & Duncan, M. J. The long-term dynamical behavior of short-period comets. *Icarus* **108**, 18–36 (1994).
55. Brož, M., Vokrouhlický, D., Morbidelli, A., Nesvorný, D. & Bottke, W. F. Did the Hilda collisional family form during the late heavy bombardment? *Mon. Not. R. Astron. Soc.* **414**, 2716–2727 (2011).
56. Vokrouhlický, D. Diurnal Yarkovsky effect as a source of mobility of meter-sized asteroidal fragments. I. Linear theory. *Astron. Astrophys.* **335**, 1093–1100 (1998).
57. Vokrouhlický, D. & Farinella, P. The Yarkovsky seasonal effect on asteroidal fragments: a nonlinearized theory for spherical bodies. *Astron. J.* **118**, 3049–3060 (1999).
58. Čapek, D. & Vokrouhlický, D. The YORP effect with finite thermal conductivity. *Icarus* **172**, 526–536 (2004).
59. Farinella, P., Froeschlé, C. & Gonczi, R. Meteorite delivery and transport. *IAU Symp.* **160**, 205–222 (1994).
60. Alí-Lagoa, V. et al. Differences between the Pallas collisional family and similarly sized B-type asteroids. *Astron. Astrophys.* **591**, A14 (2016).
61. Brož, M. & Morbidelli, A. A study of 3-dimensional shapes of asteroid families with an application to Eos. *Icarus* **317**, 434–441 (2019).
62. Benz, W. & Asphaug, E. Impact simulations with fracture I—Method and tests. *Icarus* **107**, 98–116 (1994).
63. Jutzi, M., Holsapple, K., Wünneman, K. & Michel, P. in *Asteroids IV* (eds Michel, P. et al.) 679–699 (Univ. Arizona Press, 2015).

64. Ševeček, P. et al. SPH/*N*-body simulations of small ($D=10$ km) asteroidal breakups and improved parametric relations for Monte-Carlo collisional models. *Icarus* **296**, 239–256 (2017).
65. Richardson, D. C., Quinn, T., Stadel, J. & Lake, G. Direct large-scale *N*-body simulations of planetesimal dynamics. *Icarus* **143**, 45–59 (2000).
66. Tillotson, J. H. *Metallic Equations of State for Hypervelocity Impact* GA–3216 (General Dynamics, 1962).
67. von Mises, R. Mechanik der festen krper im plastisch- deformablen zustand. *Nachr. Ges. Wiss. Gott. Math. Phys. Klasse* **4**, 582–592 (1913).
68. Grady, D. & Kipp, M. Continuum modelling of explosive fracture in oil shale. *Int. J. Rock. Mech. Min. Sci.* **17**, 147–157 (1980).
69. Benz, W. & Asphaug, E. Simulations of brittle solids using smooth particle hydrodynamics. *Comput. Phys. Commun.* **87**, 253–265 (1995).
70. Bottke, W. F. & Greenberg, R. Asteroidal collision probabilities. *Geophys. Res. Lett.* **20**, 879–881 (1993).
71. Bottke, W. F. et al. Linking the collisional history of the main asteroid belt to its dynamical excitation and depletion. *Icarus* **179**, 63–94 (2005).
72. Benz, W. & Asphaug, E. Catastrophic disruptions revisited. *Icarus* **142**, 5–20 (1999).
73. Vilas, F. & Gaffey, M. J. Phyllosilicate absorption features in main-belt and outer-belt asteroid reflectance spectra. *Science* **246**, 790–792 (1989).
74. Fornasier, S., Lantz, C., Barucci, M. A. & Lazzarin, M. Aqueous alteration on main belt primitive asteroids: results from visible spectroscopy. *Icarus* **233**, 163–178 (2014).
75. Cloutis, E. A. et al. Spectral reflectance properties of carbonaceous chondrites 4: aqueously altered and thermally metamorphosed meteorites. *Icarus* **220**, 586–617 (2012).
76. Lantz, C. et al. Ion irradiation of carbonaceous chondrites: a new view of space weathering on primitive asteroids. *Icarus* **285**, 43–57 (2017).
77. Rivkin, A. S., Asphaug, E. & Bottke, W. F. The case of the missing Ceres family. *Icarus* **243**, 429–439 (2014).
78. Castillo-Rogez, J. et al. Insights into Ceres's evolution from surface composition. *Meteorit. Planet. Sci* **53**, 1820–1843 (2018).
79. Howard, K. T., Benedix, G. K., Bland, P. A. & Cressey, G. Modal mineralogy of CM chondrites by X-ray diffraction (PSD-XRD): Part 2. degree, nature and settings of aqueous alteration. *Geochim. Cosmochim. A* **75**, 2735–2751 (2011).
80. Alí-Lagoa, V. et al. Physical properties of B-type asteroids from WISE data. *Astron. Astrophys.* **554**, A71 (2013).
81. Castillo-Rogez, J. C. et al. Iapetus' geophysics: rotation rate, shape, and equatorial ridge. *Icarus* **190**, 179–202 (2007).
82. Schmidt, B. E. & Castillo-Rogez, J. C. Water, heat, bombardment: the evolution and current state of (2) Pallas. *Icarus* **218**, 478–488 (2012).
83. Opeil, C. P., Consolmagno, G. J. & Britt, D. T. The thermal conductivity of meteorites: new measurements and analysis. *Icarus* **208**, 449–454 (2010).
84. Dufresne, E. R. & Anders, E. On the chemical evolution of the carbonaceous chondrites. *Geochim. Cosmochim. A* **26**, 1085–1114 (1962).
85. Bland, P. A. & Travis, B. J. Giant convecting mud balls of the early Solar System. *Sci. Adv.* **3**, e1602514 (2017).
86. Carry, B. et al. Homogeneous internal structure of CM-like asteroid (41) Daphne. *Astron. Astrophys.* **623**, A132 (2019).
87. Alí-Lagoa, V. et al. Differences between the Pallas collisional family and similarly sized B-type asteroids. *Astron. Astrophys.* **591**, A14 (2016).
88. Hanuš, J. et al. Shape, size, physical properties and nature of low-perihelion near-Earth asteroid (3200) Phaethon. In *Proc. 48th AAS Division for Planetary Sciences Meeting* 516.08 (American Astronomical Society, 2016).
89. Masiero, J. R., Wright, E. L. & Mainzer, A. K. Thermophysical modeling of NEOWISE observations of DESTINY$^+$ targets phaethon and 2005 UD. *Astron. J.* **158**, 97 (2019).
90. Kareta, T. et al. Rotationally resolved spectroscopic characterization of near-Earth object (3200) Phaethon. *Astron. J.* **156**, 287 (2018).
91. Ito, T. et al. Extremely strong polarization of an active asteroid (3200) Phaethon. *Nat. Commun.* **9**, 2486 (2018).
92. Cellino, A. et al. On the calibration of the relation between geometric albedo and polarimetric properties for the asteroids. *Mon. Not. R. Astron. Soc.* **451**, 3473–3488 (2015).
93. Lupishko, D. F. Generalized calibration of the polarimetric albedo scale of asteroids. *Solar Syst. Res.* **52**, 98–114 (2018).
94. Devogèle, M. et al. The phase-polarization curve of asteroid (3200) Phaethon. *Mon. Not. R. Astron. Soc.* **479**, 3498–3508 (2018).
95. Shinnaka, Y. et al. Inversion angle of phase-polarization curve of near-Earth asteroid (3200) Phaethon. *Astrophys. J. Lett.* **864**, L33 (2018).
96. Takir, D. et al. 3-μm spectroscopy of asteroid (3200) Phaethon: implications for B-asteroids. In *Proc. 49th Lunar and Planetary Science Conference* 2624 (LPI, 2018).
97. Arai, T. et al. DESTINY+ mission: flyby of Geminids parent asteroid (3200) Phaethon and in-situ analyses of dust accreting on the Earth. In *Proc. 49th Lunar and Planetary Science Conference* 2570 (LPI, 2018).
98. Gardner, J. P. et al. The James Webb Space Telescope. *Space Sci. Rev.* **123**, 485–606 (2006).

Acknowledgements

Based on observations collected at the European Organisation for Astronomical Research in the Southern Hemisphere under ESO programme 199.C-0074 (principal investigator: P.V.). This research has made use of the Keck Observatory Archive (KOA), which is operated by the W. M. Keck Observatory and the NASA Exoplanet Science Institute (NExScI), under contract with NASA. M.M. was supported by the National Aeronautics and Space Administration under grant number 80NSSC18K0849 issued through the Planetary Astronomy Program. This work was supported by the French Direction Générale de l'Armement (DGA) and Aix-Marseille Université (AMU). P.V., A.D. and B.C. were supported by CNRS/INSU/PNP. J.H., J.D. and P.S. were supported by the grant 18-09470S of the Czech Science Foundation and by the Charles University Research Programme number UNCE/SCI/023. M.Brož was supported by the grant 18-04514J of the Czech Science Foundation. E.J. is a F.R.S.-FNRS Senior Research Associate. The work of T.S.-R. was carried out through grant APOSTD/2019/046 by Generalitat Valenciana (Spain). This project has received funding from the European Union's Horizon 2020 research and innovation programme under grant agreement number 730890. This material reflects only the authors' views and the commission is not liable for any use that may be made of the information contained herein.

Author contributions

P.V. is the principal investigator of the ESO large survey that acquired the images of Pallas. M.M. and P.V. designed and operated the survey in service mode. M.M. led the research on Pallas. M.M., P.V., R.F. and T.F. reduced and deconvolved the SPHERE images. A.D. performed the crater analysis. M.Brož analysed the Pallas family and ran the N-body and SPH simulations. D.C.R and E.A. provided some of the numerical codes used for the simulations. B.C. and J.H. retrieved earlier disk-resolved and disk-integrated data for Pallas from the literature. M.V. and J.H. reconstructed the three-dimensional shape of Pallas. N.R. and L.J. analysed the shape. B.C. provided the mass estimate. J.C.-R. performed the compositional analysis and thermophysical modelling of Pallas. M.M., M.Brož, P.V. and J.C.-R. worked jointly to write the manuscript. All authors discussed the results and commented on the manuscript.

Competing interests

The authors declare no competing interests.

Additional information

Supplementary information is available for this paper at https://doi.org/10.1038/s41550-019-1007-5.

Correspondence and requests for materials should be addressed to M.M.

Peer review information *Nature Astronomy* thanks Julia de Leon and the other, anonymous, reviewer(s) for their contribution to the peer review of this work.

Reprints and permissions information is available at www.nature.com/reprints.

Publisher's note Springer Nature remains neutral with regard to jurisdictional claims in published maps and institutional affiliations.